Journal of Applied Volcanology
a SpringerOpen Journal

RESEARCH Open Access

The size range of bubbles that produce ash during explosive volcanic eruptions

Kimberly Genareau[1,2*†], Gopal K Mulukutla[3†], Alexander A Proussevitch[3†], Adam J Durant[4], William I Rose[5] and Dork L Sahagian[1†]

Abstract

Volcanic eruptions can produce ash particles with a range of sizes and morphologies. Here we morphologically distinguish two textural types: Simple (generally smaller) ash particles, where the observable surface displays a single measureable bubble because there is at most one vesicle imprint preserved on each facet of the particle; and complex ash particles, which display multiple vesicle imprints on their surfaces for measurement and may contain complete, unfragmented vesicles in their interiors. Digital elevation models from stereo-scanning electron microscopic images of complex ash particles from the 14 October 1974 sub-Plinian eruption of Volcán Fuego, Guatemala and the 18 May 1980 Plinian eruption of Mount St. Helens, Washington, U.S.A. reveal size distributions of bubbles that burst during magma fragmentation. Results were compared between these two well-characterized eruptions of different explosivities and magma compositions and indicate that bubble size distributions (BSDs) are bimodal, suggesting a minimum of two nucleation events during both eruptions. The larger size mode has a much lower bubble number density (BND) than the smaller size mode, yet these few larger bubbles represent the bulk of the total bubble volume. We infer that the larger bubbles reflect an earlier nucleation event (at depth within the conduit) with subsequent diffusive and decompressive bubble growth and possible coalescence during magma ascent, while the smaller bubbles reflect a relatively later nucleation event occurring closer in time to the point of fragmentation. Bubbles in the Mount St. Helens complex ash particles are generally smaller, but have a total number density roughly one order of magnitude higher, compared to the Fuego samples. Results demonstrate that because ash from explosive eruptions preserves the size of bubbles that nucleated in the magma, grew, and then burst during fragmentation, the analysis of the ash-sized component of tephra can provide insights into the spatial distribution of bubbles in the magma prior to fragmentation, enabling better parameterization of numerical eruption models and improved understanding of ash transport phenomena that result in pyroclastic volcanic hazards. Additionally, the fact that the ash-sized component of tephra preserves BSDs and BNDs consistent with those preserved in larger pyroclasts indicates that these values can be obtained in cases where only distal ash samples from particular eruptions are obtainable.

Background

Explosive volcanic eruptions can result in significant hazards to people and property due to the generation of pyroclastic density currents, emission of ash into the atmosphere, and deposition of ash at great distances from the source volcano. The aviation industry is at particular risk from ash-producing explosive eruptions, as demonstrated by the recent eruptions of Eyjafjallajökull (2010) and Grímsvötn (2011) in Iceland, and Puyehue-Cordón Caulle in Chile (2011). Due to considerable reliance on air transport for global commerce and travel, even relatively small explosive eruptions can have far-reaching consequences, shutting down international and regional airports, altering airline flight paths, and resulting in large economic impacts.

Ash is the finest fraction of volcanic tephra (< 2 mm), formed from a number of different processes that may include: 1) magma-water interaction (e.g., Wohletz 1983; Zimanowski et al. 1986; Zimanowski 2001; Gonnermann

* Correspondence: genareau@gmail.com
†Equal contributors
[1]Department of Earth & Environmental Sciences, Lehigh University, 1 West Packer Avenue, Bethlehem, PA 18018, USA
[2]Department of Geological Sciences, University of Alabama, 201 7th Ave., Tuscaloosa, AL 35487, USA
Full list of author information is available at the end of the article

and Manga 2007); 2) comminution within the conduit or during the transport of pyroclastic density currents (e.g., Dufek and Manga 2008; Rose and Durant 2009a; Dufek et al. 2012); or 3) the explosive fragmentation of bubbles that nucleate and grow during magma ascent and degassing when the melt portion of the magma becomes oversaturated with dissolved volatiles, primarily H_2O (Sparks 1978; Dunbar and Hervig 1992; Gardner et al. 1996; Papale 1999; Sahagian 1999; Zhang 1999; Alidibirov and Dingwell 2000; Wallace 2002; Spieler et al. 2004; Koyaguchi and Mitani 2005). Volcanic ash represents a significant hazard to the airline industry and operation of global commerce (Casadevall 1994; Casadevall et al. 1996; Prata 2009; Durant et al. 2010), water quality (Stewart et al. 2006; Stewart et al. 2009; Wilson et al. 2010), agriculture (Cronin et al. 1997; Wilson et al. 2010), stability of local infrastructure (Wardman et al. 2012a; 2012b; Wilson et al. 2012), and human health (Baxter et al. 1999; Horwell et al. 2003a, 2003b; Hansell et al. 2006; Hincks et al. 2006; Horwell and Baxter 2006). Because ash can be transported for great distances regardless of the total volume of material actually erupted, it represents one of the farthest reaching volcanic hazards. Analysis of ash helps to assess the pyroclastic hazards and provides virtually the only information available regarding the eruption-driving bubbles that fragmented to produce the ash. By constraining the sizes of the bubbles that burst during fragmentation, it is possible to glean information regarding magma ascent and vesiculation processes, as well as to establish a correlation between eruption style and the proportion of ash generated during eruption. It is toward these goals that this research is directed.

It has been previously demonstrated that explosive volcanic eruptions are driven by the nucleation and growth of exsolved gas bubbles in the magma (Sparks 1978; Proussevitch and Sahagian 1996; 1998; 2005; Sahagian 2005; Gonnermann and Manga 2007) which leads to foam disruption due to instability of interbubble films and plateau borders, causing fragmentation (McBirney and Murase 1970; Proussevitch et al. 1993; Alidibirov 1994; Zhang 1999; Alidibirov and Dingwell 2000; Gonnermann and Manga 2007; Castro et al. 2012). Despite the necessity to understand mechanisms of ash production during explosive volcanic eruptions, knowledge is limited due to (1) the disruption of magmatic foams during fragmentation that destroys existing bubbles, and (2) the small size of the ash particles that result from energetic eruptions. Typically, lapilli-sized tephra (2–64 mm) are analyzed using either two-dimensional scanning electron/optical microscopy techniques on sectioned and polished clasts (e.g., Cashman and Mangan 1994; Klug and Cashman 1994; and Toramaru, 1990) or X-ray computed microtomography (e.g., Song et al. 2001; Shin et al. 2005; Gualda and Rivers 2006; Polacci et al. 2006, 2009; Degruyter et al. 2010a, 2010b). These methods allow examination of entire bubbles that remain preserved in erupted products (the bubbles that did not burst during fragmentation). Until now, analysis of the finest tephra fraction (ash) produced by explosive fragmentation has not been feasible, and any information regarding the bubbles that produced the resultant particles was lost. However, such information is necessary in order to understand bubble nucleation and fragmentation mechanisms that produce volcanic ash during the most energetic eruptions, toward the ultimate goal of mitigating associated immediate and long-term hazards.

In addition to concern about volcanic hazards from erupted ash, a second reason to study ash is that it results from high intensity eruptions and may shed light on the processes that lead to these cataclysmic events. In some cases it may be the only evidence of large-scale explosive eruptions at large distances from source, and it can be safely collected far from the site of the actual eruption following deposition. Although the complete bubble population can be constrained through analysis of larger pyroclasts, in some instances these larger size fractions may not be available at certain collection sites, particularly in very distal locations. As such, analysis of ash as developed here makes it possible to quantify the bubble size population in cases where *only* the ash-sized tephra component is available for study.

Here, we present the results of a study utilizing stereo-scanning electron microscopy (SSEM) that enables construction of digital elevation models (DEMs) of individual ash grains and calculation of bubble volumes from the remaining imprints using specialized software developed for this purpose (Proussevitch et al. 2011; Genareau et al. 2012). We compare SSEM analyses between ash samples from two very well-characterized volcanic eruptions of different explosivities and magma compositions to examine the utility of the microtextural method. We focus on deposits from the 14 October 1974 eruption of Volcán Fuego, Guatemala and the 18 May 1980 eruption of Mount St. Helens (MSH), Washington, U.S.A. (Figure 1). These two particular events represent two different eruptive styles (sub-Plinian and Plinian, respectively) and two different magma compositions (basalt and dacite, respectively). Their contrasting compositions may be expected to lead to differences in vesiculation and fragmentation dynamics.

Samples of tephra fall deposits from these eruptions were collected (by others) after deposition, and sieving analyses were performed in order to characterize the tephra granulometry as a function of distance from source. Differences in both the explosivities of the eruptions and the bulk magma compositions allowed a first-order comparison between different types of ash-producing volcanic events to test the viability of the SSEM method in

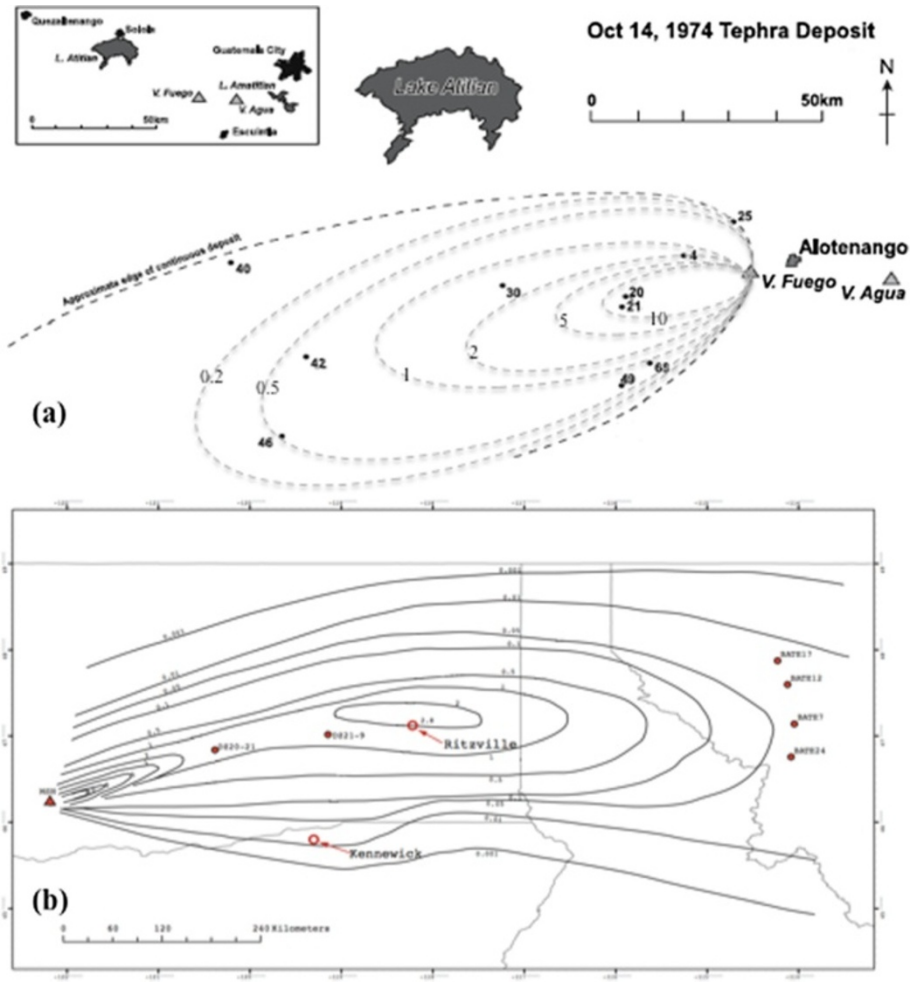

Figure 1 Collection locations of ash samples. (a) The October 14, 1974 eruption of Volcán Fuego, Guatemala (modified from Rose et al. 2008); and **(b)** the May 18, 1980 eruption of Mount St. Helens, Washington, U.S.A (modified from Durant et al. 2009).

determining the size of the bubbles that burst to produce the ash component of the tephra and helping to characterize individual eruptions. Samples utilized for this study were based on availability, and were not selected in advance due to any specific characteristics.

Eruption characteristics

14 October 1974: Volcán Fuego, Guatemala

The 14 October 1974 eruption of Volcán Fuego, Guatemala was characterized by a quasi-sustained column (rising up to ~14 km above the vent) in conjunction with multiple explosions that erupted a dense rock equivalent (DRE) of 0.021 km^3 over a period of 5 hours for an eruption rate of ~3.2×10^6 kg s^{-1} (Stoiber 1974; Rose et al. 1978; Rose et al. 2008). The tephra dispersal, total time period of the eruption, and quasi-sustained nature of the explosion classifies this particular event as sub-Plinian, as opposed to Vulcanian (Rose et al. 2008). The 14 October sub-Plinian explosion occurred in a longer sequence of events that began on 10 October and ended on 23 October, and samples from 14 October were immediately collected in the days following the eruption (Figure 1a) (Rose et al. 1978; Murrow et al. 1980; Rose et al. 2008). Juvenile tephra from this event was composed of high-Al basaltic (50% SiO_2) scoriacious ash and lapilli. Tephra deposition from this eruption included the emplacement of pyroclastic flow deposits (Davies et al. 1978; Rose et al. 2008) and ash dispersal over a total area of ~1600 km^2 (Rose et al. 2008). Grain size distribution (GSD) of the tephra fall deposit was unimodal, except in more marginal and distal locations, where the GSD became bimodal, including >10 wt% fine ash (>4 ϕ; < 63 μm) (Rose et al. 2008).

18 May 1980: Mount St. Helens, Washington, U.S.A.

The eruption of Mount St. Helens, Washington, on 18 May 1980 involved several different phases of activity, including an initial lateral blast followed by a Plinian

eruption column and then extensive pyroclastic flows, which produced co-ignimbrite plumes and a significant amount of very fine ash (>5 ϕ; < 30 μm). The 1980 magma from Mount St. Helens was dacitic (65 wt% SiO_2). The main phase of the eruption lasted almost 9 hours and produced an average mass flux of 4.4×10^7 kg s^{-1} (Carey et al. 1990; Andrews and Gardner 2009), more than an order of magnitude greater than Fuego's 14 Oct 1974 event. The height of the eruption column was between 13 and 19 km for almost 9 hours (Carey and Sigurdsson 1985; Carey et al. 1990; Andrews and Gardner 2009). Samples of tephra fall from this eruption have been extensively studied (e.g., Sarna-Wojcicki AM et al (1981); Klug and Cashman, 1994; Rose and Durant 2009b). Klug and Cashman (1994) examined pumice clasts and observed two separate bubble size modes depending upon the texture of the analyzed clast. Grey, relatively less vesicular pumice clasts with higher microlite contents displayed a BSD with an equivalent vesicle diameter mode of ~15 μm, while the more vesicular, less crystalline white pumice clasts displayed an equivalent vesicle diameter mode of ~50 μm. Analyses of the ash component of the 1980 MSH tephra showed that 50 wt% of the total GSD was comprised of very fine ash (< 30 μm) (Rose and Durant 2009b). As indicated by these previous studies, explosive eruptions of various styles, with different magma compositions, can produce various proportions of ash and other pyroclasts based on the size and number density of bubbles that control the nature of fragmentation.

Simple and complex ash particle textures

Preliminary examination of ash fall deposits revealed the existence of two texturally distinguishable types of ash-sized pyroclasts within both Fuego and MSH samples, which we refer to as simple and complex ash particles (Proussevitch et al. 2011; Genareau et al. 2012). Simple ash particles preserve, at most, one vesicle imprint on each facet of the particle. Thus, only a single bubble can be measured by the SSEM technique (Figure 2a and 2b) (Genareau et al. 2012). Complex ash particles are pumice- or scoria-like particles that preserve numerous vesicle imprints on their surfaces, and may also contain additional complete, unfragmented vesicles within their interiors (Figure 2c and 2d). Complex ash particles are much larger than the diameters of the bubbles they preserve and can be used to obtain BSD data for numerous bubbles despite only being able to "see" one side of the ash particle in an SEM image.

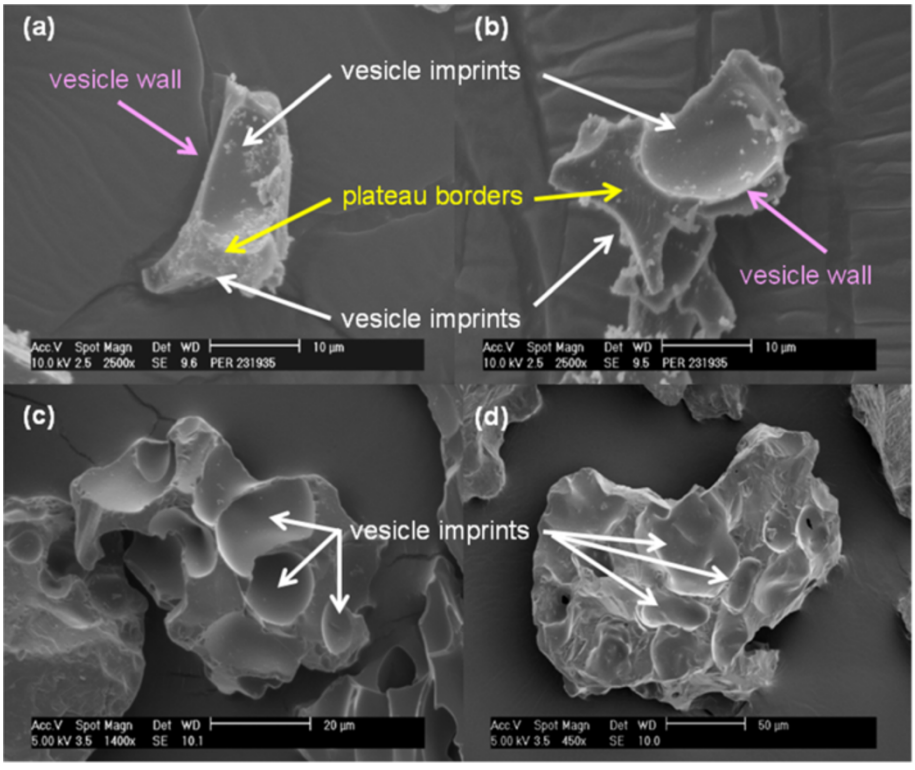

Figure 2 Features of simple and complex ash particles. (a) and **(b)** Simple ash particles from Mount St. Helens, showing partial vesicle imprints preserved adjacent to fragmented vesicle walls and plateau borders, which allow the imprint of a single vesicle to be measured per individual grain; and **(c)** and **(d)** complex ash particles, also from Mount St. Helens, which preserve the imprints of multiple vesicles on a single grain and may also contain complete, unfragmented vesicles in their interiors. Simple ash particles are typically smaller than complex ash particles.

We focus here on complex ash particles because they allow for the measurement of numerous vesicles per individual ash grain and better estimation of the number of bubble nucleation events that occurred within the magma prior to fragmentation. Because both simple and complex ash particles may exist in all tephra deposits at any distance from source, and may span a range of sizes, we make this morphological distinction to point out that only the *complex* ash particles allow for the measurement of bubbles over a broad range of sizes compared to the simple ash particles. This study complements previous work that focused on the examination of simple ash particles from the 1980 MSH eruption (Genareau et al. 2012) to determine the size of bubbles that burst to produce the very fine ash fraction (< 30 μm) of the tephra.

Methods

Sample preparation

Ash fall deposits were obtained from researchers who had collected samples on site from the 18 May 1980 eruption of Mount St. Helens, Washington, U.S.A., and the 14 October 1974 sub-Plinian eruption of Volcán Fuego, Guatemala. Grain size distribution (GSD) analyses for all of the samples used are provided in Figure 3 in addition to where the samples utilized in this study fall within the total grain size distribution (TGSD) for both eruptions as previously published. Portions of each ash sample were sonicated in deionized H_2O to separate the finer size fraction from the coarser size fraction. For both the Fuego and MSH samples, the finer portion that remained suspended in the H_2O was decanted (<30 μm) and the coarser portion was retained in order to examine the complex ash particles, which represent a greater proportion of the coarser ash fraction. Following sonication, samples were oven-dried at 60°C for 24 to 72 hours and mounted on carbon tape applied to a Hitachi 12.5 mm sample stub. After application of an iridium coat ranging from 5 to 15 nm, samples were imaged using the Philips FEI XL30 stereo-scanning electron microscope (SSEM) housed within

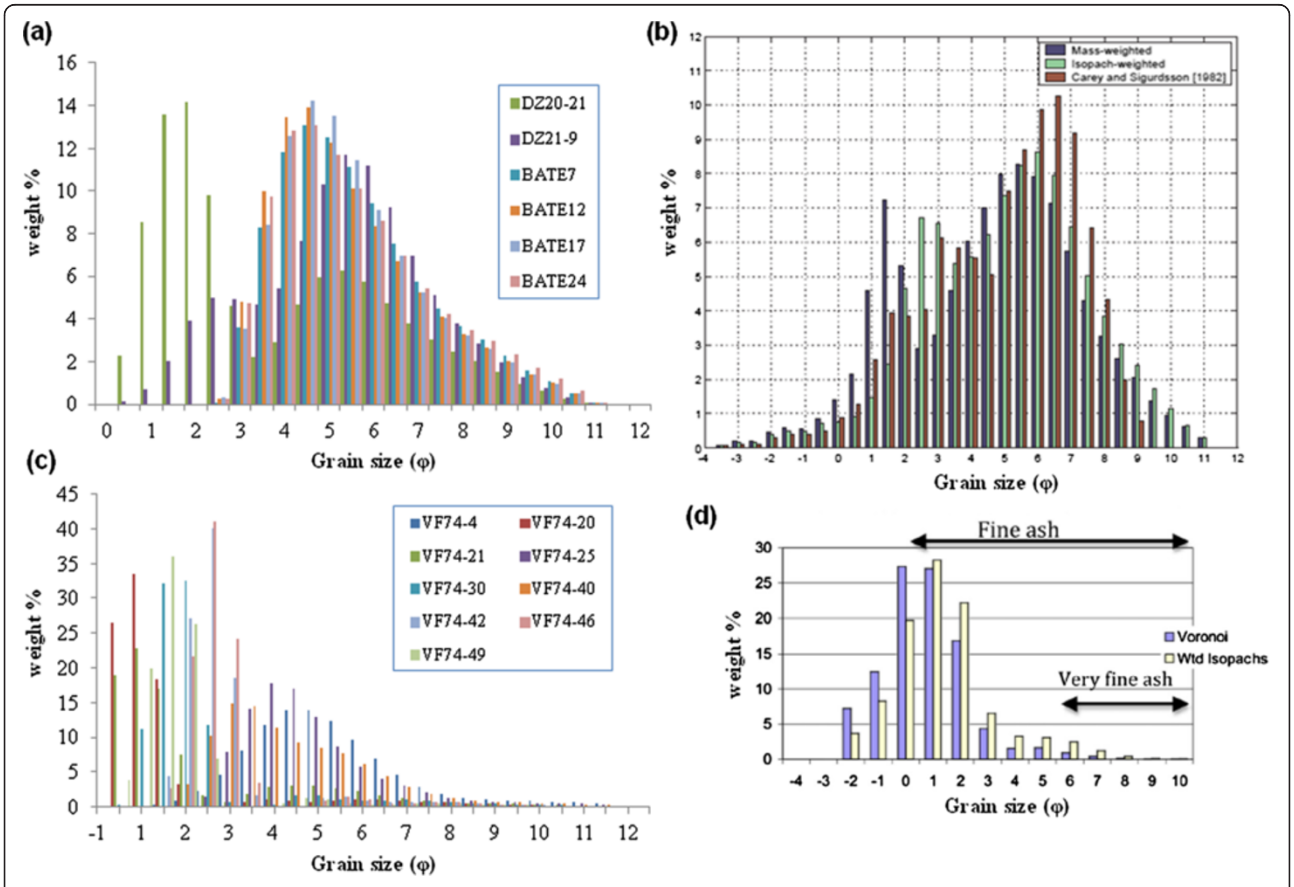

Figure 3 Results of grain size distribution (GSD) analyses for the examined samples. (a) Mount St. Helens 1980 distal samples (157–634 km from source), with GSD carried out using a Malvern Instruments Mastersizer 2000 at the University of Cambridge; **(b)** total grain size distribution (TGSD) of the fall deposit from Durant et al. (2009); **(c)** GSD of the Fuego October 14, 1974 samples, obtained through standard sieving techniques, all collected within 60 km of source (there are no data available for sample VF74-68); **(d)** TGSD of the fall deposit from Rose and Durant (2009a, 2009b). GSDs of the samples used in this study reflect the loss of larger pyroclasts with distance from source.

the Department of Materials Science and Engineering at Lehigh University.

SSEM analysis

Individual grains are selected based upon their relative position to other particles on the sample mount and their own specific characteristics. Ideal candidates are unobstructed by neighbouring grains and display curved vesicle surfaces oriented orthogonal to the electron beam, allowing acquisition of the vesicle depth in addition to the diameter. Vesicle imprints contain finer-grained material in order to provide reference points for creation of the DEM, but are not completely filled, for this would obscure true vesicle depth (Figure 4a), which is critical for DEM construction. If grain surfaces are obliquely tilted relative to the electron beam (Figure 4b) or are too close to neighbouring grains, the resulting DEM may be skewed towards inaccurate representations of vesicle depth, so vesicle imprints are selected carefully for DEM construction. There are several things to consider when performing SSEM analyses of ash grains and measurement of vesicle volumes. First, because each sample mount may contain hundreds of individual ash grains, we are only able to measure vesicle imprints on a small percentage of the grain population, thus the selection of grains for imaging is solely at the discretion of the researcher based upon the criteria outlined previously, and as a result, may be somewhat subjective. Second, complex ash particles preserve numerous vesicle imprints by definition, so in order to measure a statistically significant population of vesicles (100 or more per sample site) several complex particles must be analyzed for each sample location. Third, although individual vesicles can burst at the point of fragmentation in such a way that their films and plateau borders produce multiple ash particles, it is not possible to determine how many ash grains must be reassembled to accurately reconstruct the original bubble volume, and there is no hope of finding the various ash fragments that came from a particular bubble. Thus, we take the vesicle imprint we measure to be the sole representation of the original bubble. Finally, SSEM analyses allow only one side of the ash grain to be imaged and only the bubbles on the viewable side of the particle to be quantified. The opposite side may preserve other measureable vesicles, but it is not possible to manipulate individual grains in situ to observe multiple facets of the same ash particle. Because all samples are ash-sized grains, any particle less than 2 mm in diameter is available for analysis. However, the Fuego complex ash particles were generally larger than the MSH complex ash particles due to the more proximal locations of the Fuego samples to source and typically range in size from 50 to several hundreds of μm in diameter. Comparatively, the majority of MSH complex ash particles analyzed range from 50 to 100 μm in diameter due to the more distal sample locations utilized.

The XL30 SSEM was utilized to examine ash grains at magnifications of 100 to 10,000 times. For magnifications of 3000 times or less, a 5 kV accelerating voltage was used, but at higher magnifications, a 10 kV accelerating voltage was employed. Depending upon the magnification, the working distance varied from 9 to 11 mm. Secondary electron images of individual ash grains were collected with the sample stage at three angles: horizontal (angle of stage tilt = 0°), +3° from horizontal, and -3° from horizontal. This eucentric tilting method (Piazzesi 1973; Proussevitch et al. 2011) was utilized to collect three images of the grain at the angles described above, and these images were loaded into the Alicona MeX software (Alicona Imaging GmbH, Graz, Austria). MeX

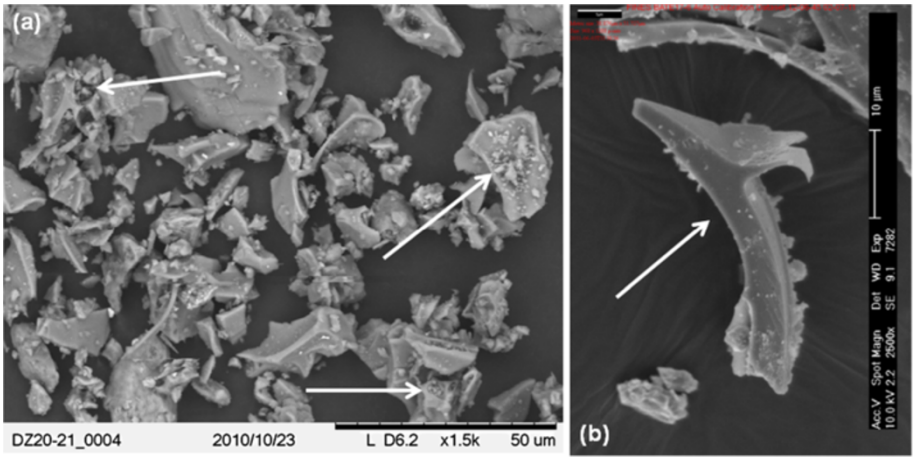

Figure 4 Examples of ash particles not suitable for the use of stereo-scanning electron microscopy. (a) Vesicle imprints completely filled with finer-grained material; and **(b)** vesicle imprints oriented perpendicular to the electron beam, both of which inhibit an accurate measurement of vesicle depth (indicated with arrows).

creates two stereo-pair anaglyphs (one from the middle and left image, one from the middle and right image), which are then combined to create a digital elevation model (DEM) of the ash surface (Figure 5). Full details of the processing method are described in Proussevitch et al. (2011).

Bubble volumes

Using BubbleMaker software (Proussevitch et al. 2011), profiles of each vesicle are selected by hand and the MeX-constructed DEM provides the length of that profile and the depth of the vesicle imprint it transects (Figure 6), allowing calculation of the original bubble volume. Calculated volumes are subsequently used to determine the bubble size distributions (BSDs) (Proussevitch et al. 2007). Secondary electron images of the measured complex ash particles were then used to determine the maximum observable particle diameter and the aspect ratios (longest observable axis/shortest observable axis) of the grain with ImageJ freeware (Rasband, W.S., ImageJ, U. S. National Institutes of Health, Bethesda, Maryland, USA, http://imagej.nih.gov/ij/, 1997–2012).

Results

Complex ash particles

Both simple and complex ash particles were found in all locations (Figures 7 and 8 and Additional files 1 and 2), but since complex ash particles are typically larger than simple ones, the relative proportion of complex particles decreases with distance from the vent as larger particles settle out of the plume faster (Figure 9). Further, with greater distance from the vent, the average size of the complex ash particles decreases as well (Table 1). Vesicle imprints were observed in hundreds of complex ash particles, and DEMs were constructed for many of these. In every case, imprints preserved on complex ash particles were concave; lacking convexities within observed vesicle imprints that could possibly indicate continued expansion of interior bubbles after the exterior bubbles burst during fragmentation. This confirms that the magma was behaving as an elastic solid at the point of fragmentation, with insufficient time before quenching for any further internal bubble growth due to remaining overpressure. This observation bears on models of magma rheology, but is not considered further here.

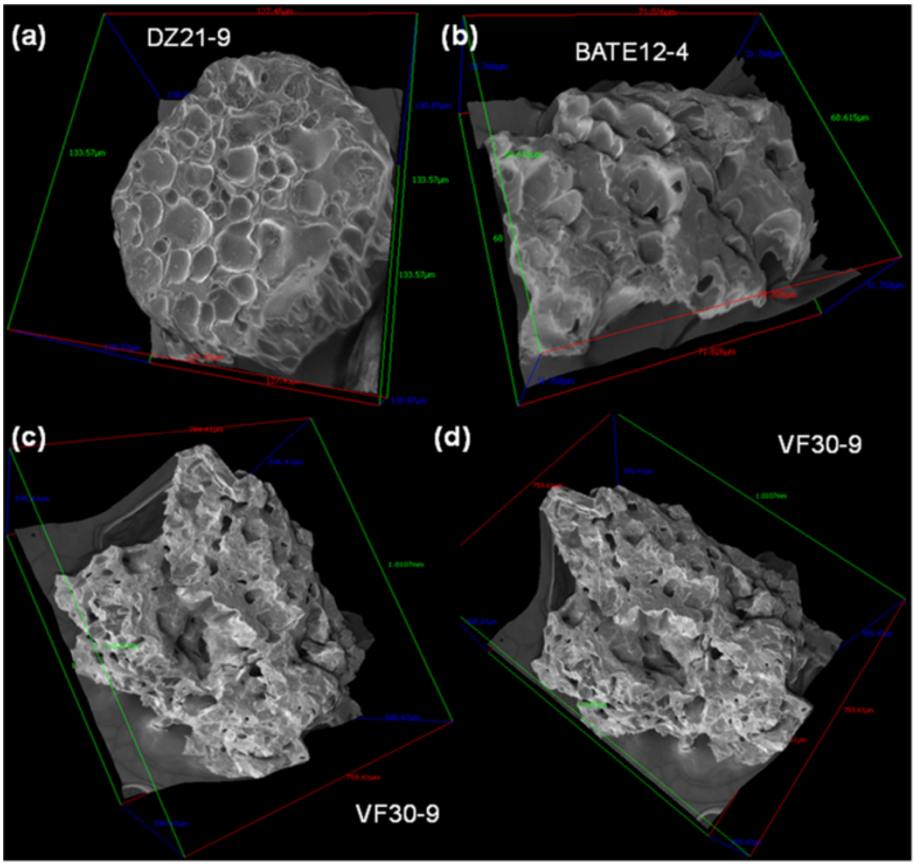

Figure 5 Digital elevation models (DEMs) of complex ash particles. (a) and **(b)** Mount St. Helens; **(c)** and **(d)** Volcán Fuego. DEMs are constructed using Alicona MeX software from two stereo-pair anaglyphs constructed from secondary electron images.

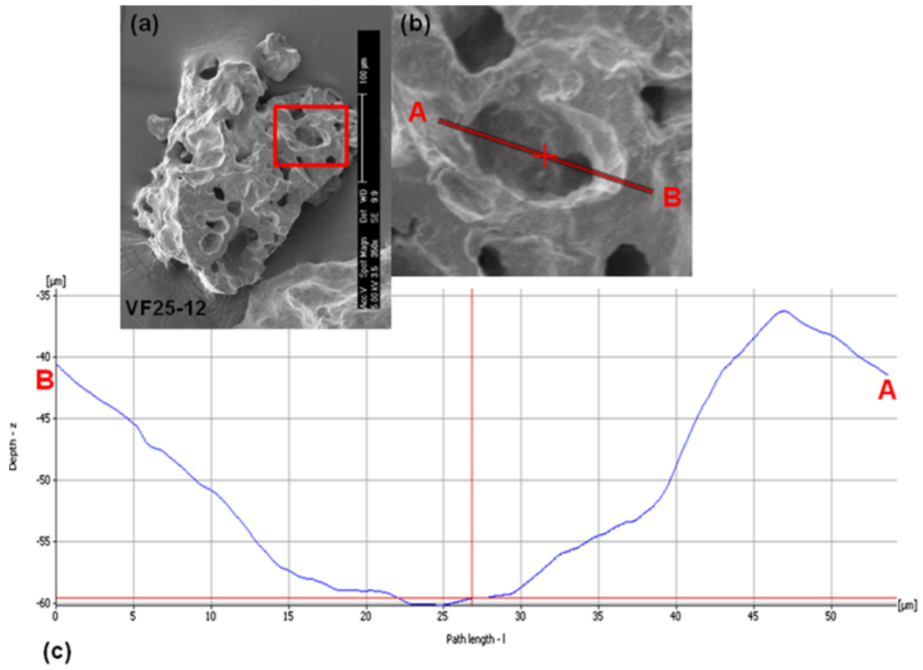

Figure 6 Profiles of vesicle imprints measured with Alicona MeX software. User-selected profiles across a vesicle imprint in a complex ash particle from Volcán Fuego, which allows BubbleMaker software to calculate the volume of the original bubble based on vesicle diameter and depth provided by the digital elevation model. **(a)** A secondary electron image of a complex ash particle from the Fuego eruption with a single vesicle imprint indicated by the red rectangle; **(b)** en enlarged view of the vesicle imprint with the selected profile across the imprint running from A to B; **(c)** length and depth of imprint as determined by the digital elevation model of the ash particle constructed using the MeX software package.

Bubble size distributions (BSD) and bubble number densities (BND)

Table 1 presents all results of the individual grain, BSD, and BND measurements for complex ash particles from both eruptions. The distance of the selected sample from source, the number of vesicles measured relative to the number of individual ash particles, and the maximum diameter and aspect ratios of the measured complex ash particles are also provided (see Additional file 3). Complex ash particles from both MSH and Fuego display bimodal BSDs (Figure 10), and we have calculated the mean, standard deviation, and total number density (TND) for a smaller bubble mode (mode 1) and a larger bubble mode (mode 2). While the number densities of smaller bubbles are several orders of magnitude higher, the contribution of the larger bubbles to the overall volume fraction is far greater. The number density distribution units are based on a logarithmic scale and defined as number of particles of a certain size per m^3 of melt/solid per the bin size given in $\log_{10}$ (m^3) units. Thus, the integration of the function fit over the domain provides bubble number density (BND), defined as the numbers of bubbles of all sizes per unit melt/solid volume, not number of bubbles per unit bulk volume (Proussevitch et al. 2007). Some of the bubbles in the Fuego complex ash particles are larger than those in the MSH complex ash particles but dominant bubble volumes do not vary with particle size (Figure 11). Both the Fuego and MSH magmas contain groundmass microlites, which also influenced vesiculation dynamics and magma rheology. Error in vesicle volume calculations are ~5-10% (Proussevitch et al. 2011).

Our BSD results from the MSH complex ash samples are consistent with previous measurement of MSH BSDs (Figure ten; Klug and Cashman 1994; Rust and Cashman 2011). Samples from both MSH and Fuego include simple and complex ash particles (see Figures 7 and 8) in all sampled locations, and the abundance of complex ash particles decrease with distance. While the sizes of the modes of the bubbles preserved by ash fragments are markedly different for the basaltic versus the dacitic eruption, many complex ash particles preserve both a larger and smaller population of bubbles. For each eruption, modal bubble size does not vary significantly with distance from the vent, although the fraction of complex ash particles capable of recording the larger bubbles decreases with distance (Figure 9). In addition, the two size modes are clearly differentiable in the MSH complex ash particles, while the Fuego samples show some overlap in the two modes (Table 1; Figure 11).

Discussion

We now consider how a complex ash particle texture may form in a fragmenting parcel of magmatic foam. If

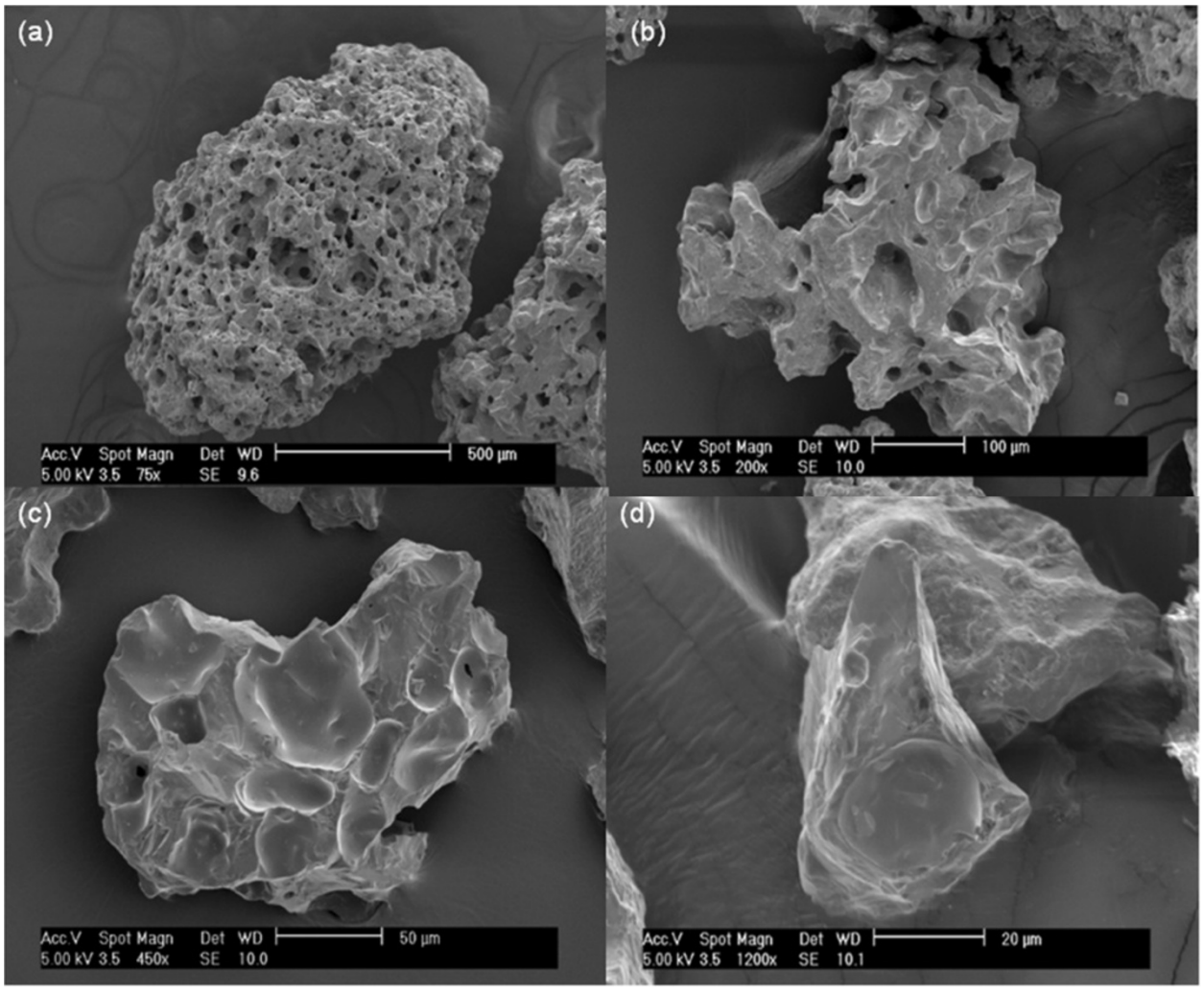

Figure 7 Ash particles from the 14 October 1974 eruption of Volcán Fuego, Guatemala. (a)-(c) Complex ash particles; **(d)** simple ash particle.

all bubbles are of identical size and evenly distributed, all bubble walls and plateau borders would disrupt simultaneously, producing only simple ash particle textures. At the opposite extreme, if all exsolving volatiles within the volcanic conduit were concentrated in a single bubble, it could burst and leave no bubbly magma behind to make complex ash particles. It is only in the realistic case of a more complex size and spatial distribution of bubbles that complex ash particles are expected to form. We interpret the complex ash particles we observe in both the MSH and Fuego deposits to result from the spatial heterogeneity produced by a later stage nucleation event of smaller bubbles within a pre-existing distribution of relatively larger bubbles.

Although smaller bubbles dominate the BND of both eruptions, MSH shows an even greater fraction of these relatively smaller bubbles than Fuego. From this we infer that the greater viscosity and lower volatile diffusivity of the MSH magma inhibited water from diffusing into pre-existing larger bubbles, thus driving relatively greater nucleation of smaller bubbles that likely formed at a comparatively later stage. Although simple ash particles can be generated from disruption of bubbles of all sizes, only complex ash particles are typically large enough to reliably record a statistically significant population of the larger bubble size mode, and it is those complex ash particles that are examined here.

The ash-sized component of proximal tephra deposits is dominated by complex ash particles, which are more likely to preserve the imprints of larger bubbles that nucleated and grew during magma ascent or formed through bubble coalescence. It is not that disruption of larger bubbles does not produce simple ash fragments, but simply that the radius of curvature of these larger bubbles cannot be distinguished (so cannot be measured) on the majority of simple ash particles due to

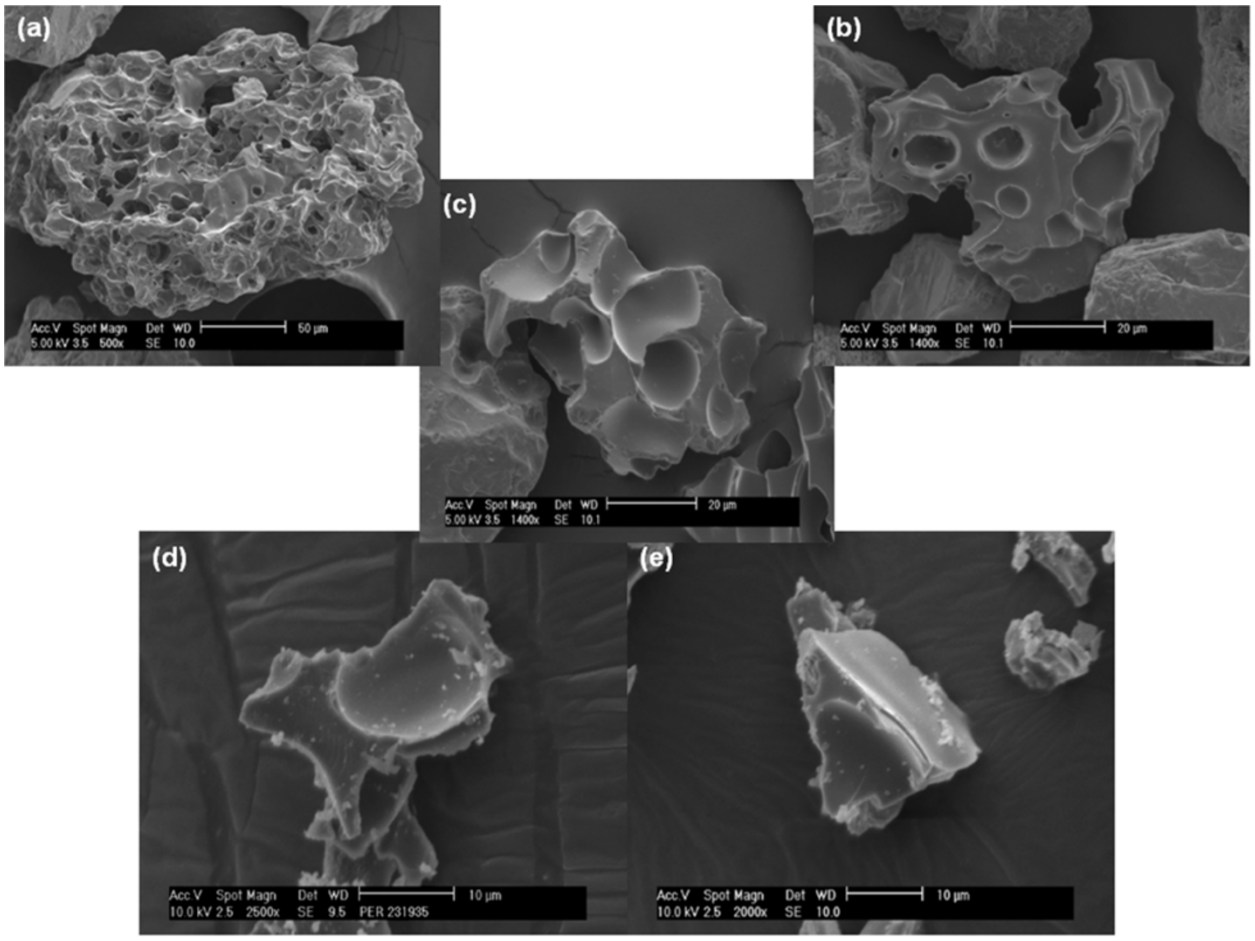

Figure 8 Ash particles from the 18 May 1980 eruption of Mount St. Helens, Washington, U.S.A. (a)-(c) Complex ash particles; **(d)** and **(e)** simple ash particles.

their relatively smaller size compared to complex ash particles. Thus, it is necessary to collect samples from proximal sites that include many complex ash particles if a statistically significant population of the larger bubbles are sought. Because we are dealing with only the ash-sized portion of the tephra, we are measuring the lower limit of the total BSD (Rust and Cashman 2011). Including the ash-sized component of tephras in the analysis of BSDs now provides an opportunity to evaluate changes in degassing and fragmentation processes between eruptive events, or throughout the course of a long-lived eruption, in order to monitor transitions in activity and potentially contribute to hazard forecasting and mitigation. For example, throughout the course of explosive activity at a particular volcano where only small volumes of ash are generated (ash venting episodes at Soufrière Hills or regular explosions at Santiaguito), if analyses of BSDs from complex ash particles show changes in bubble number densities or shifts in the size of the dominant bubble mode, this may indicate changing degassing dynamics that precede variations in eruptive style. When combined with other lines of evidence, such as seismicity or ground deformation, this information could help to forecast changes in eruptive intensity.

Inferring eruption dynamics from bubble size distributions

When a sample of ash is collected from the field, several processes must be accounted for before it can be used to elucidate eruption dynamics. Vesiculation (nucleation and bubble growth history- which is controlled by magma chemistry, volatile content, magma ascent history, and decompression path) influences the explosivity of eruption. The more viscous, silicic magmas may inhibit rapid bubble growth during ascent and thus result in smaller bubbles with greater overpressure compared to relatively less overpressured (and potentially larger) bubbles formed in more mafic magmas. Magma properties also determine the nucleation dynamics and development of smaller bubbles that form as a result of rapid, late-stage decompression. This, in turn, defines the total BSD, which combines with magma rheology and comminution to determine fragmentation efficiency. Fragmentation

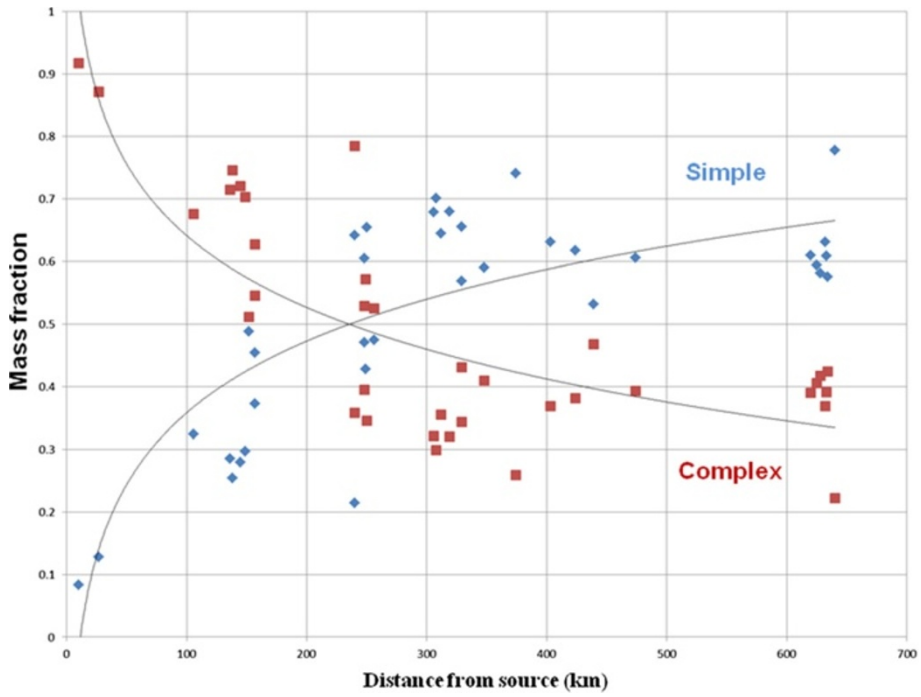

Figure 9 Relative proportions of simple and complex ash particles as a function of distance from source for the May 18, 1980 Mount St. Helens samples. Blue diamonds represent the simple ash particles while red squares represent the complex ash particles. Although both simple and complex ash particles exist in all locations, the weight fraction of complex ash particles falls from 90% to 40% at the most distal collection location due to their generally larger size compared to simple ash particles. The grey curves indicate the probability distribution function of the two morphological types with distance from source.

efficiency, in addition to comminution processes, then determines the ratio of complex to simple ash particles, which then evolves during atmospheric transport and deposition to yield the distribution collected in the field. A mono-dispersal BSD (all the same size) and homogeneous spatial distribution would produce only simple ash particles because all bubbles would burst simultaneously, while a very broad BSD curve would lead to a maximum number of complex ash particles as the largest bubbles would burst long before the growth of the smallest fraction would produce sufficient overpressure for disruption.

SSEM analysis allows quantification of bubble sizes that are larger than the ash grains on which a portion of the vesicle imprint may be preserved. In fact, a few relatively larger bubbles may be preserved on the much smaller simple ash particle surfaces (see Genareau et al. 2012), but the numbers of larger bubbles are so few relative to smaller bubbles (4 orders of magnitude less) that the few imprints they produce on simple ash particles can be neglected in a total population. Further, the radius of curvature of very large bubbles cannot be measured on simple ash particles due to their small size. Thus, analysis of complex ash particles is required to quantify the size distribution of the larger bubble population preserved in the ash-sized component of tephras, and results acquired from these complex ash particles are consistent with the lower end of the BSD curve acquired from the analyses of larger pyroclasts (Figure 10).

Timing of bubble growth inferred from size subpopulations

Once nucleated, a bubble in a rising magma grows by both diffusive addition of gas to the bubble and decompressive growth due to decrease in ambient pressure (Blank et al. 1993; Proussevitch and Sahagian 1998; Gonnermann and Manga 2007). Consequently, the size of bubbles in a magmatic foam may sometimes be used as a proxy for their age (within the variability of bubble nucleation site density). As such, a bimodal BSD is interpreted to represent at least two separate nucleation events (e.g., Blower et al. 2003). Earlier-nucleated bubbles have more time to grow and are thus larger than later-nucleated bubbles (Proussevitch and Sahagian 1996; 1998; 2005; Sahagian 2005; Gardner et al. 2009). Pre-eruptive coalescence of existing bubbles would grow and broaden the larger size mode (e.g., Klug and Cashman 1994; Gonnermann and Manga 2007; Gardner et al. 2009; Castro et al. 2012). As a parcel of magma rises to shallow levels, it accelerates and rapidly (sometimes explosively) decompresses, leading to another phase of nucleation due to the inability of dissolved water to diffuse sufficiently into previously nucleated bubbles before

Table 1 Measured characteristics of complex ash particles

Eruption	Sample	Distance from source (km)	D_{MAX} (μm)	Grain A.R.	No. of Bubbles/Particles	Mode 1*			VF	Mode 2***			CVF†	χ^2
						Mean (μ)**	Sigma (σ)**	TND (10^{12} m^{-3})		Mean (μ)**	Sigma (σ)**	TND (10^{12} m^{-3})		
MSH 1980	DZ20-21	157	304	1.3	281/4	−14.53	0.81	539.93	0.544	N/A	N/A	0.077	0.873	0.53
	DZ21-9	250	208	1.6	364/5	−14.42	0.81	415.05	0.325	−10.87	1.27	N/A	0.812	0.22
	BATE7	632	74	1.5	152/10	−14.66	0.88	530.19	0.603	N/A	N/A	N/A	0.890	0.22
	BATE12	634	89	1.7	167/15	−14.18	0.94	130.25	0.620	−10.13	0.54	0.094	0.894	0.28
	BATE17	632	74	2.2	80/4	−14.99	0.96	762.53	0.476	−12.01	0.55	5.590	0.854	0.11
	BATE24	625	71	1.9	99/9	−15.09	1.20	246.11	0.498	N/A	N/A	N/A	0.860	0.31
FUEGO 1974	VF74-25	5	241	1.5	144/16	−13.49	0.74	64.85	0.469	−11.06	0.74	0.64	0.780	0.37
	VF74-4	8	140	1.6	63/15	−14.03	1.06	49.54	0.620	−13.77	0.88	109	0.842	0.06
	VF74-20	10	1805	1.3	135/11	N/A	N/A	N/A	N/A	−12.37	0.64	29.8	N/A	0.16
	VF74-21	10	1336	1.3	76/10	N/A	N/A	N/A	N/A	−12.56	0.67	6.21	N/A	0.19
	VF74-68	16	1303	1.3	324/10	−12.82	0.85	8.86	0.301	−10.00	N/A	N/A	0.710	0.21
	VF74-49	18	896	1.3	293/10	−12.97	1.02	5.34	0.415	N/A	N/A	N/A	0.757	0.22
	VF74-30	32	898	1.4	96/16	−13.01	0.68	27.12	0.276	N/A	N/A	N/A	0.670	0.13
	VF74-42	50	452	1.1	293/10	−13.84	1.03	38.01	0.423	N/A	N/A	N/A	0.761	0.20
	VF74-40	55	194	1.3	145/13	−14.46	1.19	60.43	0.423	N/A	N/A	N/A	0.761	0.26
	VF74-46	57	490	1.4	134/11	−13.49	0.73	67.81	0.234	N/A	N/A	N/A	0.682	0.55

* Log-normal distribution type.
** $Log_{10}(m^3)$ units.
*** All distribution parameters for mode # 2 (larger bubble sub-population) are for qualitative purposes only.
† Cumulative void fraction (CVF) is calculated from the void fraction (VF) of the melt resulting from the smaller bubble population (mode #1) plus the literature values of total crystal-free vesicularity, hypothesized to dominantly reflect the void fraction resulting from the larger bubble population (mode #2). For the MSH samples a value of 0.722 was used (Klug and Cashman 1994) and for the Fuego samples, a value of 0.585 was used (Rose et al. 2008).
Summary of complex ash particle dimensions and bubble size distribution data for Volcán Fuego 1974 and Mount St. Helens 1980 eruptions, showing the distance from source of each sample, the average maximum particle diameter (D_{MAX}), the average aspect ratio (A.R.) of the ash grains, the number of bubbles measured relative to the number of ash particles examined, the sizes of the two bubble modes, and the total number density (TND) of bubbles. Data for mode 2 is presented for comparative purposes only, as the number of measurable larger bubbles was so much smaller than the number of smaller bubbles that the calculated values cannot be considered statistically reliable. The void fraction (VF) of magma is reliable for the smaller bubble population (mode 1). Using this value, in combination with measured crystal-free vesicularities from the literature, the cumulative void fraction (CVF) is calculated, and represents the void fraction of the magma at the point of fragmentation of the magmatic foam. χ2 is the function fit minimization parameter that must be less than 1.5 to achieve a minimum level of significance.

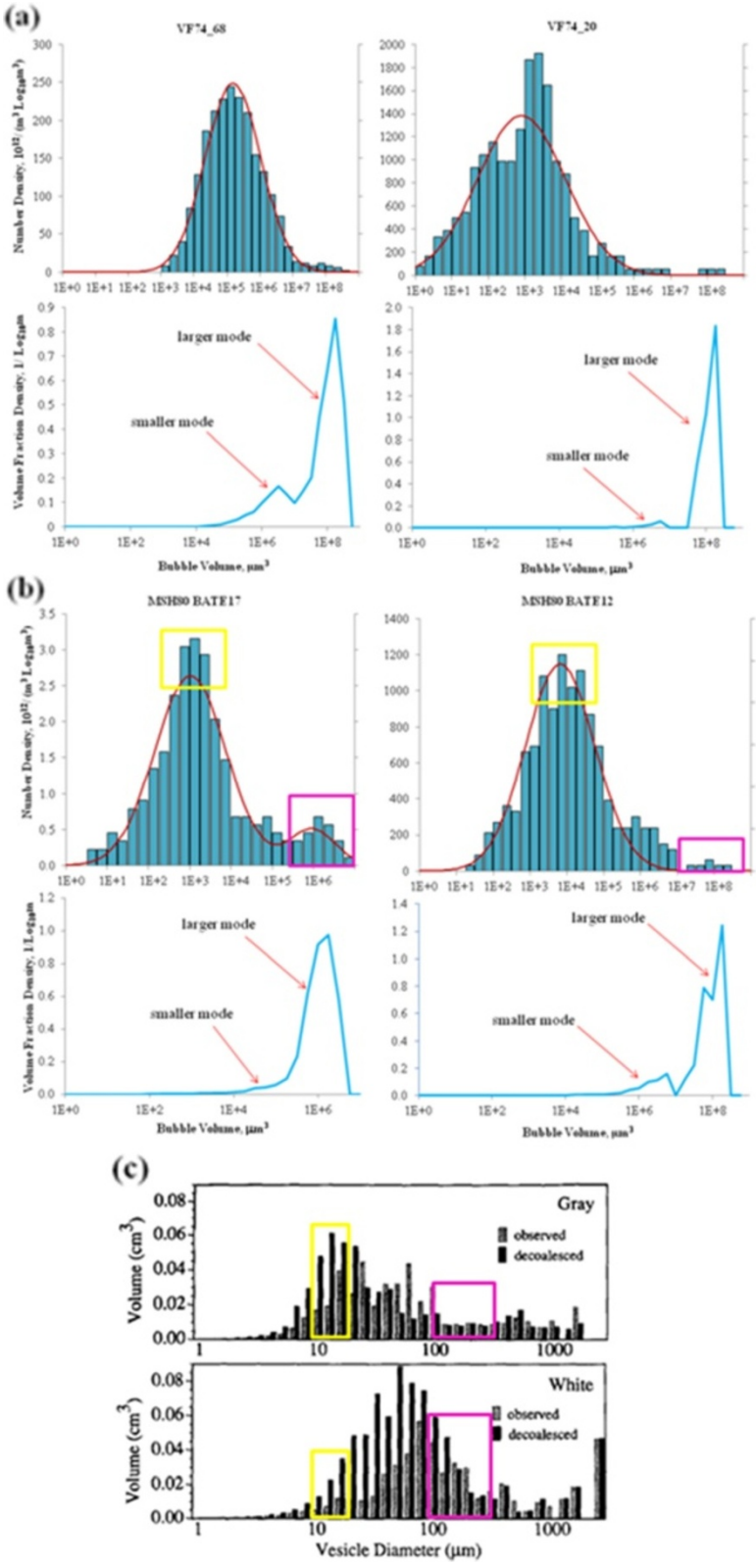

Figure 10 (See legend on next page.)

(See figure on previous page.)
Figure 10 Bubble size distributions (BSD) and bubble number densities (BND) of complex ash particles. (a) Fuego samples; and **(b)** Mount St. Helens samples. Upper plots show the number densities of the bubble volumes while the lower plots show the volume fraction density of the bubble volumes. Although the smaller bubbles dominate the number density, the larger bubbles dominate the volume fraction. The red line indicates the probability density function (function fit), which is defined in the text. In **(b)** the yellow box shows the dominant (smaller) bubble size mode while the magenta box shows the larger bubble size mode with **(c)** showing the respective bubble diameters in the distributions measured by Klug and Cashman (1994) on gray and white pumice from the 1980 Mount St. Helens eruption.

reaching oversaturation levels needed for nucleation of new bubbles (e.g., Mangan and Sisson 2000; Gonnermann and Manga 2007; Gardner et al. 2009). This late phase of bubble nucleation leads to very high bubble number densities and subsequent explosive fragmentation of a magmatic foam, leading to the generation of both simple (Genareau et al. 2012) and complex ash particles.

The detailed observations of complex ash particles reveal that there is no inflation of bubbles within the interior of ash particles subsequent to fragmentation, although it is apparent that the growth of adjacent bubbles has an influence on the final shape of vesicle walls prior to fragmentation. If post-fragmentation decompression had enabled further bubble growth within complex ash particles, bulges in at least some of the exterior bubble imprints would be expected, but are not observed. Apparently, the bubbles do not continue to expand after the complex ash particle is produced. This confirms that the highly vesiculated magmatic foam was behaving as an elastic solid at the point of fragmentation with insufficient time for viscous relaxation of any overpressure remaining in bubbles that did not burst, and thus, that fragmentation occurred within a narrow time interval that we infer to be caused by late-stage, rapid decompression.

Bubble growth in low versus high silica magma

The two cases considered in this study contrast in their eruption explosivity, and due to the Plinian nature of MSH, the very rapid decompression led to a high number density of late-stage nucleated bubbles. Larger bubbles in the MSH magma were able to expand slightly by diffusion and decompression, but late-stage nucleation of new bubbles dominated due to the low magmatic water diffusivity of dacite relative to basalt, and rate of decompression (0.9-1.6 MPa/s; e.g., Humphreys et al. 2008; Gardner 2009) induced by the preceding landslide and lateral blast, and strengthened by the positive feedback between magma ascent and degassing)). Although the processes in both eruptions were qualitatively similar, quantitatively, MSH had higher energy and greater decompression rate (e.g., Scandone and Malone 1985; Blundy and Cashman 2005), leading to a higher number density of later nucleated, smaller bubbles and higher fraction of simple ash particles than the Fuego eruption. It should be noted that there is no correlation between

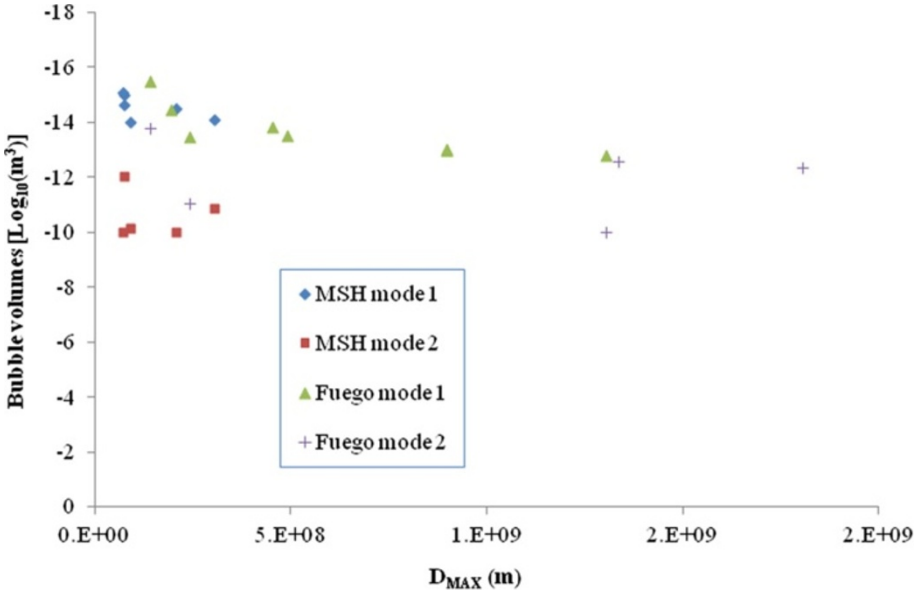

Figure 11 Plot of bubble volumes as a function of complex ash particle size. Mount St. Helens samples clearly show two modes, while Fuego samples display some overlap in the two bubble modes, which likely results from the greater range in particle size resulting from sampling of more proximal deposits compared to St. Helens samples.

the average maximum diameter of the particles and the number density of bubbles. This is due to the fact that we are dealing with complex ash particles that settled out of the plume, and represent different locations in the fragmenting magma that contained variable bubble number densities.

Ash transport distance

As would be expected, complex ash particles fall out of the plume closer to the vent due to their greater size and higher settling velocity. This causes the ash fraction composed of complex ash particles to rapidly decrease with distance from source (Figure 9). This distance, and variations in this distance between different eruptions, is presumably controlled by eruption rate differences and cloud characteristics, including GSD, eruptive column height, effectiveness of particle removal (e.g., through aggregation), prevailing wind, humidity, and other atmospheric conditions (Durant and Rose 2009, Rose and Durant 2009a, 2009b). Conversely, travel distance for simple ash particles may be very far-reaching (Genareau et al. 2012), although most simple ash particles fall out quickly and prematurely, governed by microphysical processes which are effective in the first day of atmospheric residence (see Durant et al. 2009; Durant and Rose 2009; Rose and Durant 2009a, 2009b).

This study demonstrates that the location of the collected ash sample in relation to the overall distance from the vent affects the proportions of bubble populations (larger vs. smaller bubble modes) preserved as vesicle imprints on collected ash grain surfaces. At locations farther from source, there are reduced proportions of complex ash particles, which are more likely to preserve a greater range of bubble size populations, relative to simple ash particles (Figure 9). The MSH samples were all acquired from distal locations (closest location 157 km from the vent), while the Fuego samples were necessarily obtained from more proximal and medial locations (< 60 km). Fuego samples contain not only more complex ash particles, but those complex ash particles are comparatively larger than the MSH complex ash particles and preserve a greater fraction of the relatively larger bubble population. We interpret this to reflect not only a function of sampling location, but also a lower decompression rate of the Fuego eruption, and/or lower viscosity of the Fuego magma that allowed for more rapid diffusive and decompressive growth of existing bubbles, thus reducing the oversaturation of the inter-bubble melt and the number density of later-nucleating bubbles. These results indicate that if tephras are collected at more proximal and medial locations to the vent, larger size populations within the BSD can be examined, but if tephras are only collected at distal locations, BSDs will be dominated by the final stage of bubble nucleation and growth because with greater distance from source the ash particle size decreases far below the size of the larger bubbles.

Conclusions

Explosive volcanism generates two types of morphologically distinct ash particles suitable for the utilization of SSEM imaging in order to calculate bubble volumes. Simple ash particles allow the measurement of only a single vesicle on each observable ash grain surface (Genareau et al. 2012) while relatively larger, complex ash particles preserve the imprints of multiple vesicles for measurement on a single ash grain surface and may also contain complete, unfragmented vesicles in their interiors. Both simple and complex ash particles are produced in eruptions of contrasting style and composition (Fuego: basaltic, sub-Plinian and MSH: dacitic, Plinian). The complete population of simple and complex ash particles escapes the vent, but complex ash particles fall out of the column and plume much more rapidly due to their relatively larger size, causing simple ash particles to dominate in more distal deposits. With the proportion of simple ash particles generated by fragmentation of later-nucleated bubbles increasing with distance from the vent, the apparent fraction of smaller bubbles also increases with distance. Consequently, as samples are collected from more distal deposits relative to source, measured BSDs will reflect the lower end of the total BSD for the entire eruptive unit.

Observed bubble size distributions are bimodal for both the MSH and Fuego eruptions, suggesting *at least two* bubble nucleation events in the vesiculating magma during ascent and eruption. We interpret the larger of these modes to represent bubbles that nucleated at relatively greater depth within the conduit and grew by diffusive decompression and expansion while the smaller mode nucleated at a relatively later stage of magma ascent and vesiculation.

Number densities of the smaller bubble population in the MSH complex ash particles are greater than those preserved in the Fuego complex ash particles, and the cumulative void fraction (CVF) of the MSH melt (0.864 ± 0.030) was greater than that of the Fuego melt (0.749 ± 0.051), consistent with the expectation that eruptions of greater explosivity should generate a higher number density of smaller bubbles just prior to fragmentation of the magmatic foam (Table 1). These results reflect the higher viscosity resulting from a more volatile-rich and more silicic magma, greater decompression rate, and thus, greater eruption explosivity for the MSH 1980 event. The results presented here demonstrate that SSEM analysis of ash particles can quantify the lower end of the total BSD of a pyroclastic unit, even if distal ash deposits are the *only* available data source.

Constraints on some outstanding problems regarding eruption dynamics emerge from this study. The first is that vesicles of various sizes are preserved on ash grains, and indicate that bubble nucleation occurs in more than one stage (including one very late in the eruption, just prior to fragmentation). The second is that fragmentation occurs over a short time interval in a highly vesiculated magmatic foam, leading to the production of both complex and simple ash particles simultaneously from a heterogeneous spatial distribution of bubbles. The relative abundance of complex and simple ash particles may be controlled in part by the scale of heterogeneity of bubble nucleation sites and thus the spatial distribution of bubbles and the strength of inter-bubble films and plateau borders. Quantification of this for magmas of various compositions and crystallinities would be a fruitful area for future investigation.

Methodologically, the use of SSEM enables the examination of volcanic tephra and the quantification of vesicle properties that were heretofore unavailable to researchers using previously established methods of particle imaging such as standard two-dimensional SEM examination of sectioned and polished lapilli, and X-ray microtomography of clasts or portions of clasts. SSEM enables direct measurement of the finest tephra component, the ash fraction, and quantification of BSDs for bubbles that burst during eruption and efficiently fragmented the magma as it exited the vent. For explosive eruptions where magma is efficiently fragmented to produce a high proportion of ash, the ability to quantify the ash-producing population of bubbles can reveal syn-eruptive processes of magma vesiculation and fragmentation, which is vital for understanding eruptive dynamics, parameterization of numerical eruption models, and assessment and mitigation of pyroclastic hazards.

Additional files

Additional file 1 **Secondary electron images of measured complex ash particles from the October 14, 1974 eruption of Volcán Fuego, Guatemala, obtained from sample collection site VF74-30.**

Additional file 2 **Secondary electron images of measured complex ash particles from the May 18, 1980 eruption of Mount St. Helens obtained from sample collection site DZ21-9.**

Additional file 3 **Complex ash particle dimensions for all of the samples examined in this study.**

Competing interests
There are no competing interests.

Authors' contributions
All authors contributed to this work. All authors read and approved the final manuscript.

Acknowledgements
The authors thank William Mushock and Robert Keyse for assistance with the SSEM system at Lehigh University. This project was supported by NSF grants #EAR-0838314 and EAR-0838292. These awards were funded under the American Recovery and Reinvestment Act of 2009 (ARRA). Insightful comments from Jacopo Taddeucci, Alain Burgisser, and an anonymous reviewer greatly improved the quality of the manuscript.

Author details
[1]Department of Earth & Environmental Sciences, Lehigh University, 1 West Packer Avenue, Bethlehem, PA 18018, USA. [2]Department of Geological Sciences, University of Alabama, 201 7th Ave., Tuscaloosa, AL 35487, USA. [3]Complex Systems Research Center, University of New Hampshire, 8 College Road, Durham, NH 03824, USA. [4]Norwegian Institute for Air Research, P.O. Box 100 2027, Kjeller, Norway. [5]Department of Geological Engineering and Sciences, Michigan Technological University, 1400 Townsend Drive, Houghton, MI 49931, USA.

Received: 20 February 2013 Accepted: 1 August 2013
Published: 22 Aug 2013

References
Alidibirov M (1994) A model for viscous magma fragmentation during volcanic blasts. Bull Volcanol 56:459–465
Alidibirov M, Dingwell DB (2000) Three fragmentation mechanisms for highly viscous magma under rapid decompression. J Volcanol Geotherm Res 100:413–421
Andrews BJ, Gardner JE (2009) Turbulent dynamics of the 18 May 1980 Mount St. Helens eruption column. Geology 37:895–898
Baxter PJ, Bonadonna C, Dupree R, Hards VL, Kohn SC, Murphy MD, Nichols A, Nicholson RA, Norton G, Searl A, Sparks RSJ, Vickers BP (1999) Cristobalite in volcanic ash of the Soufriere Hills Volcano, Montserrat, British West Indies. Science 283:1142–1145
Blank JG, Stolper EM, Carroll MR (1993) Solubilities of carbon dioxide and water in rhyolitic melt at 850-degrees-C and 750 bars. Earth Planet Sci Lett 119:27–36
Blower JD, Keating JP, Mader HM, Phillips JC (2003) The evolution of bubble size distributions in volcanic eruptions. J Volcanol Geotherm Res 120:1–23
Blundy J, Cashman KV (2005) Rapid decompression-driven crystallization recorded by melt inclusions from Mount St. Helens volcano. Geology 33:793–796
Carey S, Sigurdsson H (1985) The May 18, 1980 eruption of Mount St. Helens 2. Modeling of dynamics of the Plinian phase. J Geophys Res 90:2948–2958
Carey S, Sigurdsson H, Gardner JE, Criswell W (1990) Variations in column height and magma discharge during the May 18, 1980 eruption of Mount St. Helens. J Volcanol Geotherm Res 43:99–112
Casadevall TJ (1994) The 1989/1990 eruption of Redoubt Volcano Alaska: impacts on aircraft operations. J Volcanol Geotherm Res 62:301–316
Casadevall TJ, Delos Reyes PJ, Schneider DJ (1996) The 1991 Pinatubo eruptions and their effects on aircraft operations. In: Newhall CG, Punongbayan RS (eds) Fire and mud: eruptions and lahars of Mount Pinatubo. University of Washington Press, Philippines, pp 625–636
Castro JM, Burgisser A, Schipper I, Mancini S (2012) Mechanisms and dynamics of bubble coalescence in silicic magmas. Bull Volcanol: 74:2339-2352
Cronin SJ, Hedley MJ, Smith G, Neall VE (1997) Impact of Ruapehu ash fall on soil and pasture nutrient status. 1. October 1995 eruptions. New Zealand J Agricult Res 40:383–395
Cashman KV, Mangan MT (1994) Physical aspects of magma degassing, II, Constraints on vesiculation processes from textural studies of eruptive products. Rev in Mineral 30:446–478
Davies DK, Quearry MW, Bonis SB (1978) Glowing avalanches from the 1974 eruption of the volcano Fuego, Guatemala. Geol Soc Amer Bull 89:369–384
Degruyter W, Bachmann O, Burgisser A (2010a) Controls on magma permeability in the volcanic conduit during the climactic phase of the Kos Plateau Tuff eruption (Aegean Arc). Bull Volcanol 72:63–74
Degruyter W, Burgisser A, Bachmann O, Malaspinas O (2010b) Synchrotron X-ray microtomography and lattice Boltzmann simulations of gas flow through volcanic pumices. Geosphere 6:470–481
Dufek J, Manga M (2008) In situ production of ash in pyroclastic flows. J Volcanol Geotherm Res 113, B09207
Dufek J, Manga M, Patel A (2012) Granular disruption during explosive volcanic eruptions. Nature Geosci 5:561–564

Dunbar NW, Hervig RL (1992) Volatile and trace-element composition of melt inclusions from the lower Bandelier Tuff- Implications for magma chamber processes and eruptive style. J Geophys Res 97:15151–15170

Durant AJ, Rose WI (2009) Sedimentological constraints on hydrometeor-enhanced particle deposition: 1992 Eruptions of Crater Peak, Alaska. J Volcanol Geotherm Res 186:40–59

Durant AJ, Bonadonna C, Horwell CJ (2010) Atmospheric and Environmental Impacts of Volcanic Particulates. Elements 6:235–240

Durant AJ, Rose WI, Sarna-Wojcicki AM et al (2009) Hydrometeor-enhanced tephra sedimentation: Constraints from the 18 May 1980 eruption of Mount St. Helens. J Geophys Res 114, B03204

Gardner JE (2009) The impact of pre-existing gas on the ascent of explosively erupted magma. Bull Volcanol 71(8):835

Gardner JE, Thomas RME, Jaupart C, Tait S (1996) Fragmentation of magma during Plinian volcanic eruptions. Bull Volcanol 58:144–162

Gardner JE, Hilton M, Carroll MR (1999) Experimental constraints on degassing of magma: isothermal bubble growth during continuous decompression from high pressure. Earth Planet Sci Lett 168:201–218

Genareau K, Proussevitch AA, Durant AJ, Mulukutla G, Sahagian DL (2012) Sizing up the bubbles that produce very fine ash during explosive volcanic eruptions. Geophys Res Lett 39, L15306

Gonnermann HM, Manga M (2007) The fluid mechanics inside a volcano. Annu Rev Fluid Mech 39:321–356

Gualda GAR, Rivers M (2006) Quantitative 3D petrography using x-ray tomography: Application to Bishop Tuff pumice clasts. J Volcanol Geotherm Res 154:48–62

Hansell AL, Horwell, CJ, Oppenheimer C (2006) The health hazards of volcanoes and geothermal areas. Occupat and environ med 63:149-156

Hincks TK, Aspinall WP, Baxter PJ, Searl A, Sparks RSJ, Woo G (2006) Long term exposure to respirable volcanic ash on Montserrat: a time series simulation. Bull Volcanol 68:266–284

Horwell CJ, Baxter PJ (2006) The respiratory health hazards of volcanic ash: a review for volcanic risk mitigation. Bull Volcanol 69:1-24

Horwell CJ, Fenoglio I, Ragnarsdottir KV, Sparks RSJ, Fubini B (2003a) Surface reactivity of volcanic ash from the eruption of Soufrière Hills volcano, Montserrat, West Indies with implications for health hazards. Environ Res 93:202–215

Horwell CJ, Sparks RSJ, Brewer TS, Llewellin EW, Williamson BJ (2003b) Characterization of respirable volcanic ash from the Soufrière Hills volcano, Montserrat, with implications for human health hazards. Bull Volcanol 65:346–362

Humphreys MCS, Menand T, Blundy JD, Klimm K (2008) Magma ascent rates in explosive eruptions: constraints from H2O diffusion in melt inclusions. Earth Planet Sci Lett 270:25–40

Klug C, Cashman KV (1994) Vesiculation of May 18, 1980, Mount St. Helens Magma. Geology 22:468–472

Koyaguchi T, Mitani NK (2005) A theoretical model for fragmentation of viscous bubbly magmas in shock tubes. J Geophys Res 110:B10202.1–B10202.21

Mangan M, Sisson T (2000) Delayed, disequilibrium degassing in rhyolite magma: decompression experiments and implications for explosive volcanism. Earth Planet Sci Lett 183:441–455

McBirney AR, Murase T (1970) Factors governing the formation of pyroclastic rocks. Bull Volcanol 34:372–384

Murrow PJ, Rose WI, Self S (1980) Determination of the total grain size distribution in a vulcanian eruption column, and its implications to stratospheric aerosol perturbation. Geophys Res Lett 7:893–896

Papale P (1999) Strain-induced magma fragmentation in explosive eruptions. Nature 397:425–428

Piazzesi G (1973) Photogrammetry with the scanning electron microscope. J Phys E: Sci Instrum 6:392–396

Polacci M, Baker DR, Mancini L, Tromba G, Zanini F (2006) Three-dimensional investigation of volcanic textures by X-ray microtomography and implications for conduit processes. Geophys Res Lett 33:L13312

Polacci M, Baker DR, Mancini L, Favretto S, Hill RJ (2009) Vesiculation in magmas from Stromboli and implications for normal Strombolian activity and paroxysmal explosions in basaltic systems. J Geophys Res 114, B01206

Prata AJ (2009) Satellite detection of hazardous volcanic clouds and the risk to global air traffic. Nat Haz 51(2):303–324

Proussevitch AA, Mulukutla GK, Sahagian DL (2011) A new 3D method of measuring bubble size distributions from vesicle fragments preserved on surfaces of volcanic ash particles. Geosphere 7:62–69

Proussevitch AA, Sahagian DL (1996) Dynamics of coupled diffusive and decompressive bubble growth prior to volcanic eruption. J Geophys Res 101:17447–17456

Proussevitch AA, Sahagian DL (1998) Dynamics and energetics of bubble growth in magmas: Analytical formulation and numerical modelling. J Geophys Res 103:18223–18251

Proussevitch AA, Sahagian DL (2005) Bubbledrive-1: A numerical model of volcanic eruption mechanisms driven by disequilibrium magma degassing. J Volcanol Geotherm Res 143:89–111

Proussevitch AA, Sahagian DL, Kutolin V (1993) Stability of foams in silicate melts. J Volcanol Geotherm Res 59:161–178

Proussevitch AA, Sahagian DL, Tsentalovich EP (2007) Statistical analysis of bubble and crystal size distributions: Formulations and procedures. J Volcanol Geotherm Res 164:95–111

Rose WI, Anderson AT, Woodruff LG, Bonis SB (1978) The October 1974 basaltic tephra from Fuego volcano: description and history of the magma body. J Volcanol Geotherm Res 4:3–53

Rose WI, Durant AJ (2009a) Fine ash content of explosive eruptions. J Volcanol Geotherm Res 186:32–39

Rose WI, Durant AJ (2009b) El Chichón volcano, 4 April 1982: Volcanic cloud history and fine ash fallout. Nat Haz 51:363–374

Rose WI, Murrow PJ, Bonadonna C, Durant AJ, Ernst GGJ (2008) Nature and significance of small volume fall deposits at composite volcanoes: Insights from the October 14, 1974 Fuego eruption, Guatemala. Bull Volcanol 70(9):1043–1067

Rust AC, Cashman KV (2011) Permeability controls on expansion and size distributions of pyroclasts. J Geophys Res 116, B11202

Sahagian DL (1999) Magma fragmentation during volcanic eruptions. Nature 402:589–591

Sahagian DL (2005) Volcanic eruption mechanisms: Insights from intercomparison of models of conduit processes. J Volcanol Geotherm Res 143:1–16

Sarna-Wojcicki AM et al (1981) Areal distribution, thickness, mass, volume, and grain size of air-fall ash from the six major eruptions of 1980. In: Lipman PW, Mullineaux DR (eds) The 1980 Eruptions of Mount St. Helens. U. S. Geological Survey, Washington, pp 577–600

Scandone R, Malone SD (1985) Magma supply, magma discharge and readjustment of the feeding system of Mount St. Helens during 1980. J Volcanol Geotherm Res 23:239–262

Shin H, Lindquist WB, Sahagian DL, Song SR (2005) Analysis of the vesicular structure of basalts. Comput Geosci 31:473–487

Song SR, Jones KW, Lindquist WB, Dowd BA, Sahagian DL (2001) Synchrotron X-ray computed microtomography: studies on vesiculated basaltic rocks. Bull Volcanol 63:252–263

Sparks RSJ (1978) The dynamics of bubble formation and growth in magmas: A review and analysis. J Volcanol Geotherm Res 3:1–38

Spieler O, Kennedy B, Kueppers U, Dingwell DB, Scheu B, Taddeucci J (2004) The fragmentation threshold of pyroclastic rocks. Earth Planet Sci Lett 226:139–148

Stewart C, Johnston DM, Leonard GS, Horwell CJ, Thordarson T, Cronin SJ (2006) Contamination of water supplies by volcanic ashfall: A literature review and simple impact modelling. J Volcanol Geotherm Res 158:296–306

Stewart C, Pizzolon L, Wilson TM, Leonard GS, Dewar D, Johnston DM, Cronin SJ (2009) Can volcanic ash poison water supplies? Integr Environ Assess Manage 5(4):713–716

Stoiber RE (1974) Eruption of Volcán Fuego- October 14, 1974. Bull Volcanol 38:861–869

Toramaru A (1990) Measurement of bubble size distributions in vesiculated rocks with implications for quantitative estimation of eruption processes. J Volcanol Geotherm Res 43:71–90

Wallace PJ (2002) Volatiles in submarine basaltic glasses from the Northern Kerguelen Plateau (ODP Site 1140): Implications for source region compositions, magmatic processes, and plateau subsidence. J Petrol 43:1311–1326

Wardman JB, Wilson TM, Bodger PS, Cole JW, Johnston DM (2012a) Investigating the electrical conductivity of volcanic ash and its effect on HV power systems. J Phys Chem of the Earth 45–46:128–145

Wardman JB, Wilson TM, Bodger PS, Cole JW, Stewart C (2012b) Potential impacts from tephra fall to electric power systems: A review and mitigation strategies. Bull Volcanol 74(10):2221–2241

Wilson TM, Stewart C, Cole J, Johnston D, Cronin SJ (2010) Vulnerability of agricultural water supplies to volcanic ash fall. Environ Earth Sci 61(4):675–688

Wilson TM, Stewart C, Sword-Daniels V, Leonard GS, Johnston DM, Cole JW, Wardman J, Wilson G, Barnard ST (2012) Volcanic ash impacts on critical infrastructure. J Phys Chem of the Earth 45–46:5–23

Wohletz KH (1983) Mechanisms of hydrovolcanic pyroclast formation: grain-size, scanning electron microscopy, and experimental studies. J Volcanol Geotherm Res 17:31–63

Zhang Y (1999) A criterion for the fragmentation of bubbly magma based on brittle failure theory. Nature 402:648–650
Zimanowski B, Lorenz V, Frohlich G (1986) Experiments on phreatomagmatic explosions with silicate and carbonatitic melts. J Volcanol Geotherm Res 30:149–153
Zimanowski B (2001) Phreatomagmatic explosion. In: Freundt A, Rosi M (eds) From Magma to Tephra. Elsevier Science, New York, pp 25–53

10.1186/2191-5040-2-4
Cite this article as: Genareau *et al.*: The size range of bubbles that produce ash during explosive volcanic eruptions. *Journal of Applied Volcanology* 2013, 2:4